



HAL
open science

First discoveries and localizations of Fast Radio Bursts with MeerTRAP: real-time, commensal MeerKAT survey

K.M. Rajwade, M.C. Bezuidenhout, M. Caleb, L.N. Driessen, F. Jankowski,
M. Malenta, V. Morello, S. Sanidas, B.W. Stappers, M.P. Surnis, et al.

► **To cite this version:**

K.M. Rajwade, M.C. Bezuidenhout, M. Caleb, L.N. Driessen, F. Jankowski, et al.. First discoveries and localizations of Fast Radio Bursts with MeerTRAP: real-time, commensal MeerKAT survey. *Mon.Not.Roy.Astron.Soc.*, 2022, 514 (2), pp.1961-1974. 10.1093/mnras/stac1450 . hal-03703969

HAL Id: hal-03703969

<https://hal.science/hal-03703969v1>

Submitted on 12 Apr 2023















HAL is a multi-disciplinary open access archive for the deposit and dissemination of scientific research documents, whether they are published or not. The documents may come from teaching and research institutions in France or abroad, or from public or private research centers.

L'archive ouverte pluridisciplinaire **HAL**, est destinée au dépôt et à la diffusion de documents scientifiques de niveau recherche, publiés ou non, émanant des établissements d'enseignement et de recherche français ou étrangers, des laboratoires publics ou privés.



Distributed under a Creative Commons Attribution 4.0 International License

First discoveries and localizations of Fast Radio Bursts with MeerTRAP: real-time, commensal MeerKAT survey

K. M. Rajwade ^{1,2}★ M. C. Bezuidenhout,¹ M. Caleb ^{1,3,4} L. N. Driessen,⁵ F. Jankowski ¹,
M. Malenta,¹ V. Morello ¹ S. Sanidas,¹ B. W. Stappers,¹ M. P. Surnis ¹ E. D. Barr ⁶ W. Chen ⁶,
M. Kramer ^{1,6} J. Wu,⁶ S. Buchner ⁷ M. Serylak ^{8,9} F. Combes,¹⁰ W. Fong,¹¹ N. Gupta ¹²,
P. Jagannathan ¹³ C. D. Kilpatrick ¹¹ J.-K. Krogager,¹⁴ P. Noterdaeme,^{15,16} C. Núnñez,¹⁷
J. Xavier Prochaska,^{18,19} R. Srianand ¹² and N. Tejos¹⁷

Affiliations are listed at the end of the paper

Accepted 2022 May 19. Received 2022 May 14; in original form 2022 March 28

ABSTRACT

We report on the discovery and localization of fast radio bursts (FRBs) from the MeerTRAP project, a commensal fast radio transient-detection programme at MeerKAT in South Africa. Our hybrid approach combines a coherent search with an average field-of-view (FoV) of 0.4 deg^2 with an incoherent search utilizing a FoV of $\sim 1.27 \text{ deg}^2$ (both at 1284 MHz). Here, we present results on the first three FRBs: FRB 20200413A ($DM = 1990.05 \text{ pc cm}^{-3}$), FRB 20200915A ($DM = 740.65 \text{ pc cm}^{-3}$), and FRB 20201123A ($DM = 433.55 \text{ pc cm}^{-3}$). FRB 20200413A was discovered only in the incoherent beam. FRB 20200915A (also discovered only in the incoherent beam) shows speckled emission in the dynamic spectrum, which cannot be explained by interstellar scintillation in our Galaxy or plasma lensing, and might be intrinsic to the source. FRB 20201123A shows a faint post-cursor burst of about 200 ms after the main burst and warrants further follow-up to confirm whether it is a repeating FRB. FRB 20201123A also exhibits significant temporal broadening, consistent with scattering, by a turbulent medium. The broadening exceeds from what is predicted for the medium along the sightline through our Galaxy. We associate this scattering with the turbulent medium in the environment of the FRB in the host galaxy. Within the approximately 1 arcmin localization region of FRB 20201123A, we identify one luminous galaxy ($r \approx 15.67$; J173438.35-504550.4) that dominates the posterior probability for a host association. The galaxy's measured properties are consistent with other FRB hosts with secure associations.

Key words: stars:neutron – radio continuum: transients.

1 INTRODUCTION

Fast radio bursts (FRBs) are bright radio flashes of hitherto unknown origin. They last for less than a few milliseconds and their dispersion measures (DMs), the integrated electron densities along the lines of sight, far exceed the contributions from our own Galaxy, indicating their cosmological nature (Lorimer et al. 2007; Thornton et al. 2013). FRBs are therefore potentially new probes to study the cosmic history of the Universe and are currently in use to probe important cosmological milestones (e.g. Macquart et al. 2020). Since their discovery in 2007 (Lorimer et al. 2007), more than 600 FRBs have been reported (The CHIME/FRB Collaboration et al. 2021). Initially, most FRBs were observed as one-off events, i.e. a single burst detected from a given part of the sky. The lack of multiple pulses from the same FRB suggested cataclysmic models to explain their origins (see Platts et al. 2019, for a full review of theories). This changed when a FRB was found to repeat (Spitler et al. 2016). This was followed by its localization to a host galaxy, confirming their extragalactic nature. Moreover, evidence of a periodicity in

the activity cycle of two repeating FRBs (Chime/Frb Collaboration et al. 2020; Rajwade et al. 2020), combined with a detection of a FRB-like radio pulse from a highly magnetized neutron star located in our Galaxy (Bochenek et al. 2020; CHIME/FRB Collaboration et al. 2020), were major breakthroughs towards constraining the progenitors of these enigmatic bursts. In the last few years, the field has progressed rapidly, owing to a slew of new repeaters discovered by the Canadian hydrogen intensity mapping experiment (CHIME), and the localizations and host galaxy identifications of many one-off FRBs discovered by the *Australian SKA Pathfinder* (ASKAP) telescope (Shannon et al. 2018). While the rate of FRB discoveries has increased tremendously, every new FRB shows interesting emission characteristics and morphology that pose more questions. For example, there is an obvious dichotomy between the spectral features and pulse widths of the repeating and one-off FRBs (Pleunis et al. 2021), but their rates are still consistent with all FRBs originating from a single underlying population (Caleb et al. 2019). This highlights the importance of discovering and following up these sources at radio, optical, and other frequencies.

Radio transient surveys have expedited progress in the field of transient astrophysics in the recent years. The use of the state-of-the-art central processing units (CPUs) and graphical processing

* E-mail: rkaustubh10@gmail.com

units (GPUs) can enable processing of high volumes of telescope data in real-time. Furthermore, with the advent of new technology, astronomers have been able to increase the field-of-view (FoV) and sensitivity of radio telescopes. All of this has led to commensal transient searches, where by the radio data taken for a different science goal are being used to look for FRBs and other radio transients. This is an important approach, especially when telescope resources are oversubscribed and a limited amount of time is available to achieve all the scientific goals. Additionally, the need to not only discover new FRBs but also to localize them and identify their host galaxies is paramount to elucidate some of these mysteries surrounding the FRB phenomenon. The MeerKAT radio telescope (Jonas & MeerKAT Team 2016) in South Africa is the ideal telescope to perform this task by the virtue of its high sensitivity to transients and excellent angular resolution to localize. MeerTRAP (*More* TRansients And Pulsars) is an ERC funded project (PI: Stappers) and has been deployed on the telescope to commensally discover and localize FRBs and other transients in real-time.

MeerTRAP piggybacks on other large survey projects (LSPs) that are using MeerKAT for science observations. During these commensal observations, MeerTRAP performs time-domain searches for transients in real-time with the primary goal of discovering and localizing FRBs in order to identify their host galaxies. The instrument was commissioned in early 2019 and has been fully operational on all LSPs at MeerKAT since September of 2020. Since then, MeerTRAP has been discovering new radio transients within and beyond the Galaxy (Bezuidenhout et al. 2022). In this paper, we present the first three FRB discoveries by the MeerTRAP instrument. The paper is organized as follows: In Section 2, we give a brief overview of the MeerTRAP project. Then, we present the new FRBs discovered and discuss some interesting emission properties for a few of them. In the next section, we discuss the localization constraints on the FRBs, specifically focusing on one of them and discuss its potential host galaxy identification. Finally, we present our discussion and summarize our results in Sections 7 and 8, respectively.

2 THE MEERTRAP SYSTEM

The MeerTRAP compute cluster also known as the transient user supplied equipment (TUSE) consists of 67 servers with one head node and 66 compute nodes located in the Karoo Array Processing Building at the MeerKAT site. Each compute node contains two Intel Xeon 8C/16T CPUs, each possessing 16 logical cores for computation, two Nvidia GeForce 1080 Ti GPUs and 256 GB of DDR4 random access memory (RAM) blocks. Each node is connected to a breakout switch via 10 GbE network interface cards (NIC) that are used to ingest data.

The signals from all the antennas are detected and summed to form an incoherent beam (IB) that samples the entire FoV of the telescope ($\sim 1.27^\circ$ at 1284 MHz). Simultaneously, signals from a subset of antennas are added by using the phase information to create a large set of narrow, highly sensitive coherent beams (CBs) that sample a fraction of the primary FoV. Typically, the coherent beams are more sensitive than the incoherent beam by a factor of ~ 5 , but cover only a fraction of the primary FoV of the telescope ($\sim 0.4 \text{ deg}^2$ at 1284 MHz). However, this fraction depends strongly on the observing frequency and elevation as the telescope array projected on the sky modifies the shape of the CBs significantly (see Chen et al. 2021, for a detailed treatment). The coherent beams' positions are determined by an algorithm that efficiently arranges them within a circular tiling region such that they intersect at a user-

Table 1. Dedispersion plan for single-pulse search pipeline.

DM range (pc cm ⁻³)	Δ DM (pc cm ⁻³)	Downsampling factor
0.00–383.75	0.307	1
383.75–774.95	0.652	2
774.95–1534.55	1.266	4
1534.55–3041.75	2.512	8
3041.75–5241.75	4.000	16

specified relative sensitivity. By default, MeerTRAP specifies that the CBs intersect at 25 per cent of their maximum sensitivity. The full details of the method used for modelling the CB point-spread function are provided in Chen et al. (2021) and further details about the full algorithm along with the verification and validation tests are being compiled as a separate paper (Bezuidenhout et al, submitted.). The incoherent and coherent beams are created in the filterbank beamformer user supplied equipment (FBFUSE) cluster that has been built by the Max Planck Institute for Radio Astronomy in Bonn (see Barr 2018, for more details). Commissioning tests in the early 2019 have shown that the beamforming efficiency at 1284 MHz is typically between 0.92–0.96, which gave us confidence that we were able to exploit almost the entire sensitivity of the array. The results of this commissioning are presented in Chen et al. (2021). Data from FBFUSE are received over the network on the NICs as SPEAD¹ packets that are read by the data ingest code and written to POSIX shared memory ring buffers of 50 s duration. The data are arranged such that each compute node ingests a number of coherent beams to be processed in real-time. Since the data from the beamformer arrive in a frequency–time format (i.e. frequency being the slowest moving axis), they are transposed to a time–frequency format on a per beam basis, as required by the transient search code. The data are also scrunched in time and frequency, resulting in an effective time resolution of 306 μ s over a band of 856 MHz that is split into 1024 channels (channel width of 208.4 kHz) and 4096 channels (channel width of 104.2 kHz), depending on the number of frequency channels that are scrunched in the beamformer. The resulting filterbank data are saved in separate shared memory buffers corresponding to each beam. Details of the MeerTRAP instrumentation have been presented in Sanidas et al. (2018), Caleb et al. (2020), Jankowski et al. (2020), Malenta et al. (2020), Rajwade et al. (2020), and a complete system overview will be given in Stappers et al. (in prep.).

The data at 1.284 GHz for each beam are searched for bright bursts using the state-of-the-art GPU-based single pulse search pipeline ASTROACCELERATE² (Armour et al. 2011; Adámek & Armour 2020). The real-time search was done by incoherently de-dispersing in the DM range 0–5118.4 pc cm⁻³, divided into multiple sub-ranges with varying DM steps and time-averaging factors (see Table 1 for details) across a bandwidth of 856 MHz with a sampling interval of 306 μ s. We also searched up to a maximum boxcar width of 0.67 s. This particular choice of parameters allowed us to process all data in real-time; thanks to strict optimizations applied in the ASTROACCELERATE algorithms.

To reduce the number of detections due to radio frequency interference (RFI), we applied a static frequency channel mask to the data before the de-dispersion and single-pulse search. While the

¹<https://casper.ssl.berkeley.edu/wiki/SPEAD>

²<https://github.com/AstroAccelerateOrg/astro-accelerate>

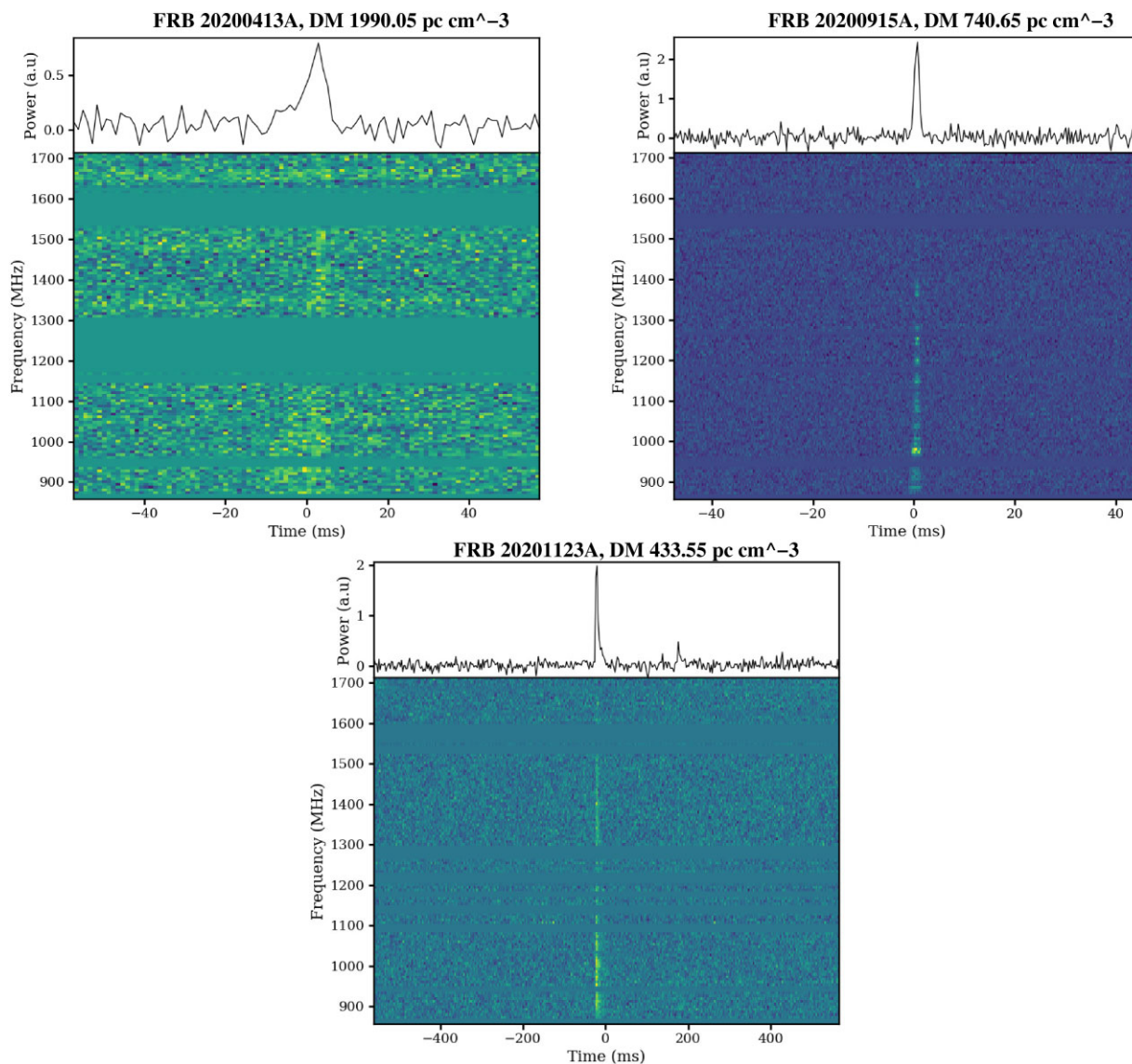


Figure 1. Dynamic spectrum of all the FRBs presented in this paper. The lower panels show the time–frequency data while the top panel shows the frequency-integrated burst profile. The pulses have been dispersed to the DM that maximizes the S/N of the detection. The horizontal lines that show the same colour are data that have been flagged due to RFI.

RFI remained stable for most of the time, the static mask did suffer from instances where the channels were corrupted by RFI varied, resulting in many spurious detections.

Additionally, the data are filtered using standard zero-DM excision (Eatough, Keane & Lyne 2009) to remove any remaining broad-band RFI that was infrequent enough not to be included in the mask. Then, the candidates are sifted based on some static cutoffs of DMs below 20 pc cm^{-3} , widths above 300 ms, and signal-to-noise (S/N) below 8.0 to reduce the number of noise or RFI candidates. The resulting candidates are then clustered using the friends-of-friends algorithm (see Huchra & Geller 1982, for more details) by combining candidates that are in close proximity in time and DM space. This resulted in a significant reduction of the total number of output candidates (~ 40 per cent). The final list of candidates are then saved to disc for further inspection. The extracted candidate files contain raw filterbank data of the dispersed pulse and additional padding of 0.5 s at the start and end of the file. This entire pipeline with all the aforementioned steps is encapsulated in a modular C++

framework called CHEETAH³, which is deployed on the compute nodes of MeerTRAP.

3 FRB DISCOVERIES

The dynamic spectra of the first three FRB discoveries are shown in Fig. 1 and the measured and derived parameters for them are presented in Table 2. We note here that beam size and shape of the CB and the IB strongly depend on the frequency and the elevation of the source. This is an important factor contributing to the FRBs being brighter in the lower half of the band and may not represent the true emission dependence on observing frequency. The three FRBs reported here are all discovered far-off the Galactic plane (gb: -50° to -10°).

³<https://gitlab.com/SKA-TDT/cheetah>

Table 2. Measured quantities for the first three FRBs discovered by MeerTRAP. Note that for FRB 20200413A and FRB 20200915A, the Right Ascension (RA) and Declination (Dec) are coordinates of the boresight of the observation and not the true position. The DMs listed here are the S/N maximized values, which are different from the value at which the burst was detected. The values in parenthesis denote the formal errors on the most significant digits.

Name	Barycentric MJD	RA ($^{\circ}$)	Dec ($^{\circ}$)	gl ($^{\circ}$)	gb ($^{\circ}$)	S/N	DM (pc cm^{-3})	Width (ms)	DM _{NE2001} (pc cm^{-3})	DM _{ymw16} (pc cm^{-3})	\mathcal{F} (Jy ms)
FRB 20200413A	58952.382356	328.57	-28.21	20.72	-50.98	14	1990.05 (88)	4.9 (2)	39.2	26.22	$\gtrsim 3.1$
FRB 20200915A	59107.105051	42.41	4.67	169.35	-47.25	35	740.65 (40)	2.2 (1)	39.1	33.72	$\gtrsim 3.0$
FRB 20201123A	59176.421148	263.67	-50.76	340.229	-9.681	45	433.55 (36)	4.6 (2)	251.93	162.4	$\gtrsim 1.4$

3.1 FRB 20200413A

This is the first FRB discovered by MeerTRAP. It was detected in the incoherent beam (IB) on UT 2020 April 13 during commensal observations of the pulsar timing experiment at MeerKAT (MeerTime; Bailes et al. 2020). The FRB was only detected in the IB, with no detections in the CB, suggesting that the FRB was outside the more sensitive CB tiling pattern. The source was detected in real-time pipeline with a S/N of 9.1 and a DM of 1988 pc cm^{-3} . The S/N and the DM were then optimized to values of 14 and $1990.05 \text{ pc cm}^{-3}$, respectively, using a custom made S/N-DM optimization code MTCUTILS.⁴ The FRB spans the entire bandwidth of the MeerKAT L-Band receiver (856–1712 MHz) and shows broadening of the pulse width at lower frequencies, probably due to the increase in the intra-channel dispersion smearing ($t_{\text{DMsmear}} \simeq 20 \text{ ms}$ at a frequency of 856 MHz for 1024 channels) and scattering. Unfortunately, the S/N of the burst is too low for a thorough analysis of this smearing.

3.2 FRB 20200915A

FRB 20200915A was discovered on UT 2020 September 15, again only in the IB. This FRB is much brighter than FRB 20200413A and was detected with a S/N of 29. Subsequent optimization of the S/N and DM with MTCUTILS showed that the FRB has S/N ratio of 35 at the best DM of $740.65 \text{ pc cm}^{-3}$. The FRB was discovered when MeerTRAP was commensally observing with the MeerKAT absorption line survey (MALS; Gupta et al. 2016) observation. The lack of CB detections meant that localizing the FRB based solely on the IB detection was not constraining. FRB 20200915A shows broadening at lower frequencies along with evidence of scintillation in the dynamic spectrum akin to what is seen in pulses from radio-emitting neutron stars in our Galaxy (for e.g. Cordes & Rickett 1998).

3.3 FRB 20201123A

FRB 20201123A was discovered on UT 2020 November 23. It was detected in a single CB with no other detections in any other neighbouring CBs or IB, making this the first discovery in the coherent beams. The burst was discovered at a S/N of 30.6 during a commensal observing run with the MeerTIME project (Bailes et al. 2020). The best optimized DM with MTCUTILS is $433.55 \text{ pc cm}^{-3}$ with a S/N of 45. The burst shows hints of scatter broadening in the bottom half of the band. Interestingly, there is a faint post-cursor seen in the time-series, separated from the main burst by $\sim 200 \text{ ms}$. The burst separation is consistent with separations observed for bursts from other repeating FRBs like FRB 20121102A (Cruces et al. 2021), suggesting that FRB 20201123A could be a repeater.

⁴<https://bitbucket.org/vmorello/mtcutils/>

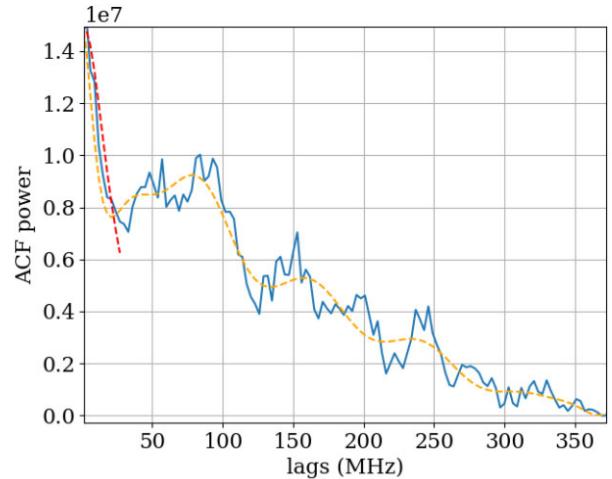


Figure 2. Autocorrelation function for FRB 20200915A as a function of lag in MHz. The red-dashed curve shows the best-fit for Lorentzian function to the very first peak after ignoring the zero-lag component that is attributed to self-noise. The orange curve shows a polynomial fit to the rest of the ACF to show the general trend of the dynamic spectrum to aid the viewer.

4 SCATTERING AND SCINTILLATION

4.1 FRB 20200915A

While FRB 20200915A does not show any obvious signatures for interstellar scattering, the dynamic spectrum clearly shows islands of band-limited emission in the lower-half of the bandwidth (Fig. 1). While this could be intrinsic to the source, such emission behaviour is typically an indication of diffractive interstellar scintillation (DISS) (Rickett 1970). In order to quantify whether this is indeed scintillation, we computed the scintillation bandwidth. To do that, we selected the dynamic spectrum (after removal of channels corrupted by RFI) for only the time bins corresponding to the on-pulse region of the burst. Then, the data were added along time axis to generate a frequency spectrum that corresponds just to the pulse integrated to a single time bin. Since the emission is dominated by the lower-half of the frequency band, we decided to perform the analysis on just the lower-half (856–1284 MHz) of the band. Then, we computed the discrete auto-correlation function (ACF) of this spectrum. For a given signal $S(\nu)$,

$$\text{ACF}(\Delta\nu) = \sum_{\nu=1}^{n_{\text{chan}}} S(\nu)\overline{S(\nu - \Delta\nu)} \quad (1)$$

where $\Delta\nu$ is the lag in the frequency axis, $S(\nu - \Delta\nu)$ is the signal at an observing frequency of $(\nu - \Delta\nu)$, and n_{chan} is the total number frequency channels. The resulting ACF is shown in Fig. 2. The decorrelation bandwidth of interstellar scintillation in the strong scattering regime is given by the full-width at half-maximum

(FWHM) of a Lorentzian function fit to the ACF (Cordes & Rickett 1998). After removing the DC component that can be attributed to self-noise of the burst itself, we fit a Lorentzian function to the ACF to obtain the $\Delta\nu_{\text{DISS}} \sim 14.75$ MHz. To compute the expected scintillation bandwidth due to our own Galaxy along the line-of-sight to this FRB, we use the NE2001 model for Galactic electron density (Cordes & Lazio 2002). The NE2001 model predicts the expected free electron density in the Galaxy based on estimates of DMs along various lines-of-sight from known radio pulsars. The predicted scintillation bandwidth is ~ 3.4 MHz, a factor of ~ 4 smaller than what is measured. We note that it is hard to gauge the significance of this deviation as no quantification of any formal model uncertainties is available currently in the literature. Hence, we can only say that assuming the model correctly predicts scintillation bandwidth, the deviation may be significant. Assuming that scintillation is caused by a thin screen with density fluctuations in the free electron density, one expects the scintles to become wider with frequency ($\Delta\nu_{\text{DISS}} \sim \nu^4$) (e.g. Lorimer & Kramer 2004). The ACF of the dynamic spectrum of FRB 20200915A along the frequency axis tells a different story. The islands of emission become visually narrower with increasing frequency, which suggests that the observed emission cannot be explained by the standard model of interstellar scintillation from our Galaxy (Majid et al. 2021). If we assume that the 14.75 MHz structure is due to scintillation from the intergalactic medium (IGM) or haloes of intersecting foreground galaxies (Prochaska et al. 2019), the corresponding scattering time-scale, $\tau_d = \frac{1}{2\pi \delta\nu_d} = 10$ ns, which is almost four orders of magnitude smaller than our finest sampling interval. While it has been shown that the IGM may not be able to contribute meaningfully to the scintillation (see Macquart & Koay 2013, and the references therein), we cannot rule out that the structures we see are due to weak scintillation and scattering from foreground haloes along the line-of-sight or the combination of the two (Ravi et al. 2016).

4.2 FRB 20201123A

The dynamic spectrum of FRB 20201123A shows evidence for scattering. To fully characterize the scattering, we divided the data into four sub-bands, each 214 MHz wide with a compromise between bandwidth and the S/N of the burst in each sub-band. We assume the scattering is caused by a thin scattering screen between the source and the observer that leads to an exponential tail in the resulting profile (see Chawla et al. 2021, and the references therein). Then, we used the SCAMP-I software suite (Oswald et al. 2021) to fit the burst profile at each frequency with an exponentially modified Gaussian.⁵ The code simultaneously fits for the scattering as well as the correction needed to the DM of the burst such that the peak of the burst under this model is aligned correctly in time after correcting for scatter broadening. The change in the DM from this fit is still consistent (within errors) with the optimized DM reported by MTCUTILS for this FRB (DM = 433.55 pc cm⁻³). The fits are performed by sampling the likelihood function of the model using MCMC (see Oswald et al. 2021, for more details). Fig. 3 shows the result of the fits. The scattering time-scale at the lowest sub-band is a factor of 2 more than the maximum expected smearing due to dispersion (4.7 ms at the lowest frequency), further supporting that the extended tail is due to scattering of the burst. The scattering time-scale for this FRB seems to follow a power law ($\tau \propto \nu^{-\alpha}$) with $\alpha = 4.2 \pm 0.4$, which is consistent with what is expected from

a scattering screen in our Galaxy based on the studies of known pulsars (Qiu et al. 2020). Despite that, the expected scattering at the best-known Galactic latitude and longitude of FRB 20201123A ($l = 340.4$, $b = -9.67$) cannot account for the scattering seen in this FRB (Cordes & Lazio 2002), which gives an expected τ of 0.016 ms at 1 GHz compared to the measured τ of 7.5 ms at 1 GHz. This points to a different source of scattering (the host galaxy or the IGM, including intersecting haloes or the combination of the two), where the medium is more turbulent than what is observed in our Galaxy (Chawla et al. 2021).

5 LOCALIZATION

For all these FRBs, we did not have visibility into data correlations between the different sets of antennas in the array available; hence, localizing the FRBs by imaging the data was not possible. Therefore, we rely on detections in the CBs and the IB to provide constraints on the location based on the best-measured model of the CB and the IB (Chen et al. 2021). We also note that the error on the beam positions is much smaller than the beamwidth, and so, negligibly contributes to the overall error on the position of the FRB. The complete methodology used and the corresponding validation and verification tests will be presented in an upcoming paper (Bezuidenhout et al., submitted.). The true position and the uncertainty of FRB 20200413A and FRB 20200915A are hard to gauge due to lack of detection in the CB, and the FRBs being located anywhere between the FWHM of the IB (1.15° at 1284 MHz) and the edge of the CB tiling (as shown in detail below).

5.1 FRB 20200413A

A detection only in the IB meant that the localization region for this FRB was unconstrained as the source could lie in any region where the IB was more sensitive than the CB (approximate CB FoV of 1.27 deg²). The exact localization region is difficult to determine as beyond the primary beam, the beam response is highly asymmetric with multiple sidelobes with varying frequency dependence. However, the smooth appearance of 20200413A's observed dynamic spectrum over a wide-band (see Fig. 1) suggests that the source is not located in a far sidelobe of the IB, as the positions of the sidelobes are strongly frequency dependent.

In order to more precisely constrain the region beyond the CB main lobes, where the FRB might have originated, we used MOSAIC (Chen et al. 2021) to generate a PSF for the CBs at various frequencies, as well as sensitivity maps of the MeerKAT primary beam obtained using astrophysical holography (e.g. Asad et al. 2021; de Villiers & Cotton 2022). The ratio of the sensitivity of a CB, S_{CB} to that of the IB, S_{IB} , at a given point is shown by

$$\frac{S_{\text{CB}}}{S_{\text{IB}}} = \frac{N_{\text{CB}}}{\sqrt{N_{\text{IB}}}}, \quad (2)$$

where $N_{\text{CB}} = 36$ and $N_{\text{IB}} = 56$ are the number of antennas used to form the CB and IB during the observation, respectively.

At each frequency, and for each CB, all coordinates were excluded as a potential origin for the FRB, where

$$S/N_{\text{CB}} > S/N_{\text{IB}} \frac{N_{\text{CB}}}{\sqrt{N_{\text{IB}}}}, \quad (3)$$

where S/N_{IB} is the measured S/N in the IB at that frequency, and S/N_{CB} is the predicted CB S/N at that frequency. Hence, all positions where any CB was more sensitive than the IB, are excluded. Viable

⁵<https://github.com/pulsarise/SCAMP-I>

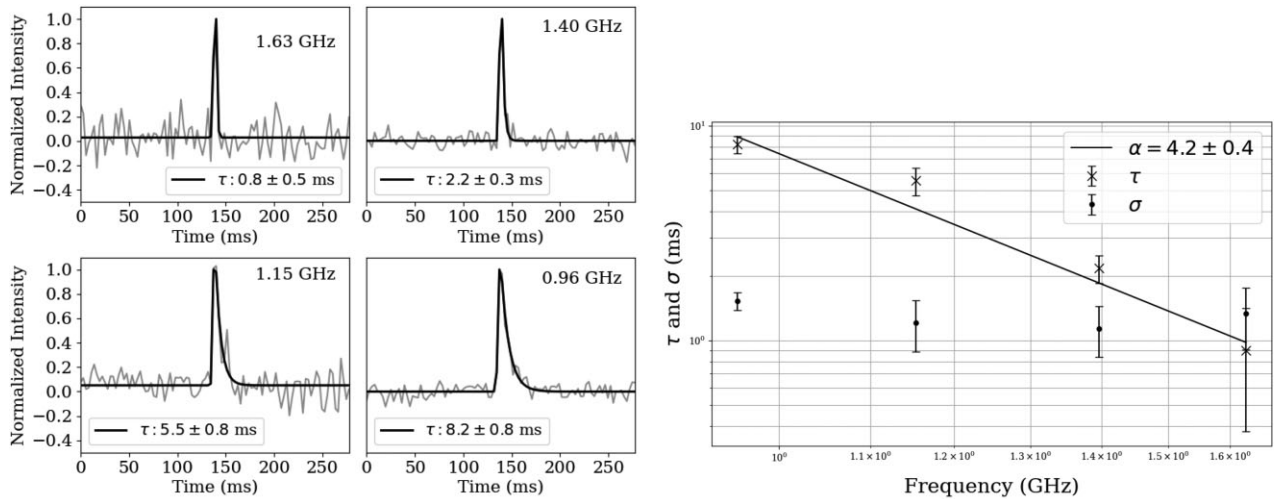


Figure 3. **Left-hand panel:** FRB 20201123A in different sub-bands (grey line) along with the best model fit to the scatter broadening (black line). Each panel shows the frequency of the sub-band. **Right-hand panel:** The variation of the scattering time-scale (τ) as a function of observing frequency. α denotes the best-fitting slope of the power-law function and the black line shows the best-fitting curve, while σ denotes the width of the Gaussian used to fit the burst at each frequency.

positions were assigned a value of 1 and excluded positions were assigned a value of 0.

This process was repeated at eight frequencies from 856 to 1605 MHz, and the resulting maps added together are shown in the left-hand panel of Fig. 4. The blue ellipsoids show the 25 per cent level⁶ of the main lobe of each CB. The colour scale corresponds to the number of sub-bands in which a given position was deemed viable; the maximum likelihood, therefore, occurs where the IB was more sensitive than all CBs in all sub-bands. This analysis indicates that the FRB most likely originated from immediately outside the CB tiling region.

5.2 FRB 20200915A

Similar to FRB 20200413A, FRB 20200915A has very little localization information as it was only detected in the IB. The result of a similar localization analysis, as performed for FRB 20200413A, is shown in the right-hand panel of Fig. 4.

Since in this case, MeerTRAP was piggybacking a MALS observation, the MeerKAT correlator saved correlations for every 8 s integration. This means that if the FRB is bright enough, it will be detected in the 8 s radio images of the field. For a pulse with a detected S/N_{td} in the time domain search, the expected S/N in the image,

$$S/N_{\text{image}} = S/N_{\text{td}} \frac{G_{\text{CB}}}{G_{\text{IB}}} \sqrt{\frac{W_{\text{td}}}{T_{\text{img}}}}, \quad (4)$$

where G_{CB} is the gain of the telescope when it is fully phased and the signals from all antennas are coherently added, G_{IB} is the gain of the incoherent sum, W_{td} the observed width of the FRB in the time-domain data, and T_{img} is the integration time of the image. For a total of 60 dishes used in the observation, we estimate $G_{\text{CB}} \simeq 2.75 \text{ K Jy}^{-1}$ and $G_{\text{IB}} \simeq 0.35 \text{ K Jy}^{-1}$. We assume here that the

⁶This number refers to the 25 per cent level of the maximum sensitivity of the CBs at the L -band centre frequency of 1.284 GHz as determined using MOSAIC.

beamforming efficiency was close to 1. Hence, for a S/N of 45 in the IB, we expect S/N_{image} of ~ 4.4 in a 8 s integration radio image.

The MALS data were processed using the automated radio telescope imaging pipeline (ARTIP). The details of ARTIP and data processing steps are provided in Gupta et al. (2021). In short, we excluded the edge frequency channels and applied a RFI mask to exclude the strong persistent RFI in the L -band. The data were then flagged and calibrated using the ARTIP-CAL package. The calibrated data were then processed using ARTIP-CONT to perform wide-band continuum imaging. For this the calibrated target, source data were averaged in frequency per 32 channels (~ 0.8 MHz) and a more stringent RFI mask to completely exclude band edges and RFI-afflicted regions was applied. Next, the resultant frequency-averaged 960 channels were regridded along the frequency axis to obtain a measurement set with 16 physically distinct spectral windows. Three rounds of phase-only and one round of amplitude and phase self-calibration were performed. For the wide-field ($6\text{k} \times 6\text{k}$ image; pixel size = 2 arcsec) broad-band imaging, the CASA task `tclean` with `w-projection` as the gridding algorithm, with 128 planes, in combination with Multi-scale Multi-term Multi-frequency synthesis (MTMFS) for deconvolution, with `nterms` = 2 and four pixel scales to model the extended emission, were used. The images were deconvolved down to 3σ using masks generated through the Python Blob Detector and Source Finder (`pyBDSF`⁷). The final continuum image, made using `robust=0` weighting, has a synthesized beam of 9.2×6.6 arcsec (position angle = -0.8°). The continuum rms is $\sim 15 \mu\text{Jy beam}^{-1}$.

For the FRB localization, we used a self-calibrated data-set, to make broad-band images for 23 time-stamps within the time range: 02:23:03.8–02:25:59.8. Since, the FRB has no signal above 1400 MHz, we considered only spectral windows 0 to 10 covering 890–1415 MHz. These $6\text{k} \times 6\text{k}$ time-stamp images (pixel size = 2 arcsec; Briggs `robust=0` weighting; Briggs 1995) at reference frequency of 1145.2 MHz typically have resolution and rms of 12.7×7.5 arcsec and $160 \mu\text{Jy beam}^{-1}$, respectively. The images were corrected for the primary beam attenuation using the model from the

⁷<https://www.astron.nl/citt/pybdsf/>

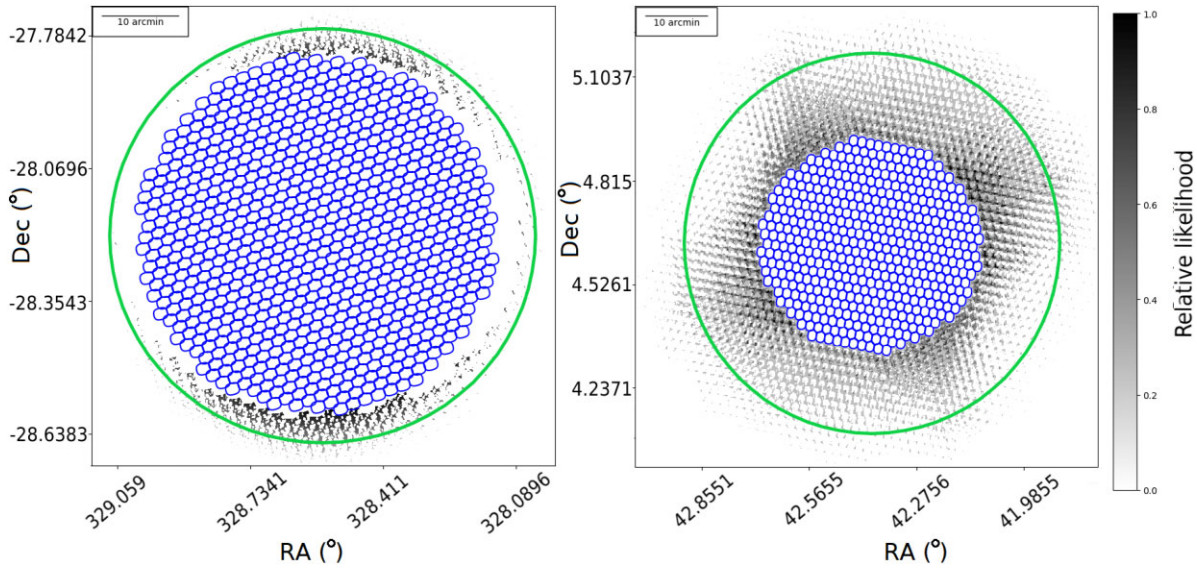


Figure 4. Likelihood greyscale map of location of FRB 20200413A (left-hand panel) and FRB 20200915A (right-hand panel). The white central region marks the area with zero probability and corresponds to the location of the coherent beam tile (shown by the blue ellipsoids), where the FRBs cannot be located as they are only detected in the IB (see text for more details). The green circle marks the FWHM of the IB at 1284 MHz. The difference in the region covered by the CB tile depends on the total number of beams that are formed and the elevation of the source.

KATBEAM library.⁸ The resulting primary beam corrected images were used for the difference imaging in order to detect a transient source. For this purpose, we used two different methods: subtracting an average image and subtracting consecutive images. We performed both of these methods for both sets of 8 s images. The average image was produced by adding all of the 23 8 s images together and dividing by 23. For the consecutive difference images, we simply subtracted the previous 8 s image from the next image. After we had produced the sets of difference images, we used `pyBDSF` to extract sources from the images. We found that the signal to noise of the extracted sources in the difference images of the time-step of the FRB, the time-step before the FRB, and the time-step after the FRB was a normal distribution centered on $S/N \sim 4$. A few S/N outliers ($S/N \gtrsim 7$) were found, but were determined to be artefacts next to bright sources. As such we were unable to distinguish which source found by `pyBDSF` in the difference images may be the FRB.

5.3 FRB 20201123A

The detection of FRB 20201123A in only a single coherent beam (FWHM of ~ 60 arcsec) does constrain its location to a 50×51 arcmin ellipse within the coherent beam using SeeKAT,⁹ a tied array beam localization algorithm designed to constrain location of bursts using detections in multiple beams (Bezuidenhout et al., submitted.). Hence, the uncertainties reported in Table 2 for FRB 20201123A are 25 arcsec in right ascension (RA) and declination (Dec). One can see that the localization region is slightly smaller than the size of the CB at 25 per cent power level, and that is because of the added constraint in the lack of detections in adjacent CBs.¹⁰ The detection in a single coherent beam with no IB

detection suggests that the expected S/N in the IB was below the detection threshold of the search pipeline. While we did not save complex voltage data for this FRB, we are able to make several inferences on its potential host galaxy. In order to do that, we try and constrain the location using Bayesian inference on the burst within this single coherent beam. The main assumption we make here is that the intrinsic spectrum of the FRB is best characterized by a power-law function. In this scenario, for a burst with an intrinsic spectral index α , the posterior probability of the offset from the boresight is

$$P(\phi, \alpha, S_i | S_o) \propto \mathcal{L}(\alpha, \phi, S_i) P(\alpha) P(\phi) P(S_i | \nu_0), \quad (5)$$

where the likelihood function is given by the following expression, having split the observing band into n equal-sized sub-bands, each with centre frequency ν_i :

$$\mathcal{L}(\alpha, \phi, S_i) = \prod_{i=0}^{n-1} \exp \left(- \frac{(S_o(\nu_i) - G(\phi, \nu_i) S_i(\nu_i))^2}{2} \right), \quad (6)$$

where $S_i(\nu_i)$ is the true integrated S/N in band i (i.e. that would have been observed had the FRB occurred on boresight), $S_o(\nu_i)$ is the observed integrated S/N in band i , ϕ is a two-dimensional vector that represents the directional offset of the FRB from the boresight of the beam and $G(\phi, \nu)$ is the beam response of the telescope. Assuming an ideal telescope receiver (i.e. a flat response of the receiver across the entire band), the S_i for a given frequency ν would scale as,

$$S_i(\nu_i) = S_i(\nu_0) \left(\frac{\nu_i}{\nu_0} \right)^\alpha, \quad (7)$$

where ν_0 is the highest frequency sub-band. The observed dynamic spectrum of FRB 20201123A can be approximated as a power law and hence that assumption is valid. In order to perform the analysis, we split the data for FRB 20201123A into four frequency sub-bands, and for each band, we computed the S/N of the detected burst. G was computed from the actual point spread function of the coherent beam where the FRB was detected. We used the MOSAIC (Chen et al. 2021)

⁸<https://github.com/ska-sa/katbeam>

⁹<https://github.com/BezuidenhoutMC/SeeKAT>

¹⁰We note that the localization region is strongly dependent on the beam spacing but for MeerTRAP, we have gone for a trade-off between the precision of localization and the total sky covered by the CB tiling.

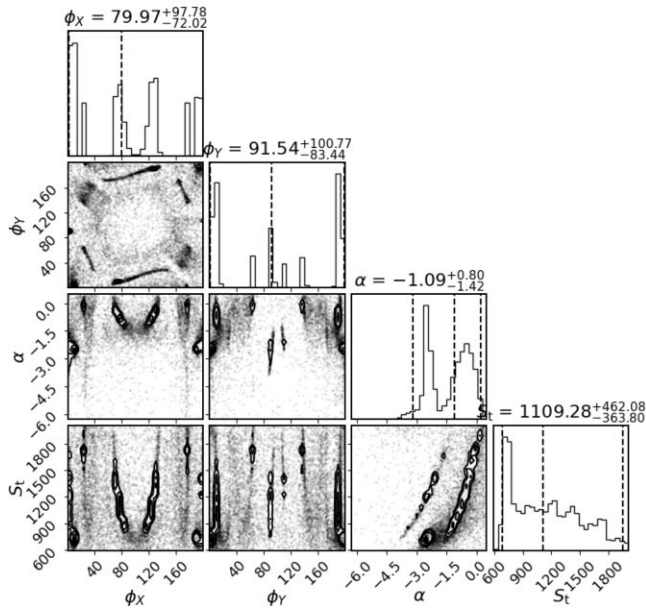


Figure 5. **Left-hand panel:** Corner–corner plot of the marginalized posterior distribution of the location of FRB 20201123A offset from the boresight (ϕ_X , ϕ_Y), the spectral index (α) and the intrinsic S/N at the highest frequency sub-band if the FRB was at the boresight of the beam (S_t). The dashed lines mark the 2.5 per cent, 50 per cent, and the 97.5 per cent credible intervals while the errors on the parameters are $2\text{-}\sigma$ (68 per cent) errors. Both ϕ_X and ϕ_Y are in units of pixels with the origin at the bottom-left corner and the resolution of 1 arcsec/pixel, such that the boresight of the beam is located at a coordinate of (100, 100). **Right-hand panel:** GMOS-S r -band image with the point-spread function of the coherent beam in which FRB 20201123A was discovered, overlaid on top (blue lines). The contours are at 0.0001 per cent, 0.4 per cent, 3 per cent, 18 per cent, and 99.9 per cent levels. The 25 per cent power level of the coherent beam is marked by the dashed white curve. One can see that the sidelobes of the beam are coincident with the primary beam of neighbouring coherent beams to rule them out as favourable locations (see text for more details). The 99 per cent confidence localization region is shown in red and the most probable host galaxy for the FRB, J173438.35-504550.4 is marked by the green ellipse.

software to generate the PSFs for various sub-bands. Each PSF is 200×200 pixels wide with a resolution of 1 arcsec/pixel. The resulting G and S/N values were fed into the Bayesian framework to compute the posterior probability of the location of the FRB as shown in Fig. 5. We used flat priors for α , ϕ , and $S_t(\nu_0)$. As one can see, the posterior distribution of ϕ_X and ϕ_Y is degenerate with multiple local maxima. This suggests that while we can characterize the spectrum of FRB 20201123A as a power law, one cannot break the degeneracy between the position of the burst in the beam and the S/N of the burst, if we assume that bursts with extremely high S/N ratios (≥ 1000) are as likely as bursts with lower S/N ratios. Constraining the higher end of the prior on S_t will only bias the posterior to favour the boresight of the beam. If there are no constraints on the priors, the 2-D posterior is expected to follow the PSF of the CB, which is exactly what is seen in the left-hand panel of Fig. 5. Those regions can be ruled out by the fact that the FRB was not seen in any adjacent coherent beam, which should have been the case if it were in any of those locations (see right-hand panel of Fig. 5). Hence, for the purposes of this analysis, the FRB is equally likely to be anywhere in the CB. This is a limitation of this technique in the case of a single beam detection. However, if the FRB is detected in multiple beams, one can compute the joint posterior distribution of the location of the burst to get more precise constraints on the location using this technique. Closely spaced beams, where the beams overlap at a significant fraction of the maximum response, will help constrain the location of the burst greatly in absence of detections in neighbouring beams. To overcome these limitations, we also decided to use another Bayesian framework to hone in on the location of the burst, and in turn, identify the possible host galaxy for FRB 20201123A, which we describe in the section below.

5.3.1 Host Association

On 2021 April 14 and 2021 May 15 UT, we obtained a series of 35×100 r -band images of the field surrounding FRB 20201123A with the Gemini multi-object spectrograph (GMOS; Hook et al. 2004) mounted on the Gemini-South telescope as part of program GS-2021A-Q-134. Given the low Galactic latitude ($b \approx -10^\circ$), the field is crowded by stars, and thus, we prioritized high image quality. These data were reduced with standard image processing techniques using the DRAGONS software.¹¹ The final stacked 3500 s image has an effective PSF FWHM of ≈ 0.64 arcsec, and it was astrometrically calibrated to match the *Gaia* DR2 catalog (Gaia Collaboration et al. 2018; Lindegren et al. 2018) with an astrometric accuracy of 0.2 arcsec.

Fig. 6 shows the ≈ 50 arcsec diameter localization of FRB 201123 on the combined r -band image. Because of the single-band detection, the localization is nearly uniform within its boundary. In this region, one expects many tens of galaxies, which challenges the association of FRB 201123 to its host galaxy. The association is further complicated by the presence of numerous stars and a Galactic extinction of $A_r \approx 1.56$ mag. However, the image reveals a single bright galaxy (hereafter, J173438.35-504550.4) towards the north-west of the region. Galaxies with its apparent magnitude ($m_r = 15.97$ mag; corrected for Galactic extinction and by the presence of an interloper star) and half-light size ($\phi \approx 2$ arcsec) are very rare, and one is intended to favour this system as the host on chance considerations alone.

¹¹<https://dragons.readthedocs.io>

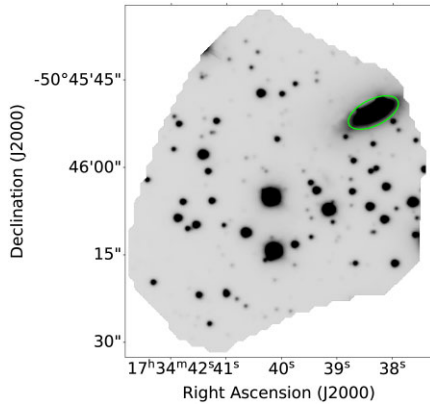


Figure 6. GMOS-S r -band image of our localization region for FRB 20201123A. The figure shows GMOS-S data only within the 99 per cent confidence region for the location of FRB 20201123A. The extended source J173438.35-504550.4 is the bright, most extended extragalactic source in the top-right of the figure and the leading candidate for the host of FRB 20201123A (green ellipse).

We proceeded to perform a probabilistic association to transient host (PATH; Aggarwal et al. 2021) analysis for FRB 20201123A. From the r -band image, we used the PHOTUTILS package (Bradley et al. 2021) to detect sources within the localization region. Table 3 lists all of these detected sources and their measured properties. Apparent magnitudes were calibrated using reference stars from the SkyMapper southern survey (Onken et al. 2019). In order to assess whether an object is a galaxy, we run SOURCE EXTRACTOR (Bertin & Arnouts 1996) and used the CLASS_STAR parameter as our star/galaxy classifier. In the following, we restrict to sources with a star/galaxy classifier value lower than 0.9 and assume the remainder are stars. Four of the sources detected by PHOTUTILS were not detected by SOURCE EXTRACTOR, and thus, these lack a star/galaxy classifier. In the following, we will conservatively assume that these are all galaxies. Last, we correct the apparent magnitudes by $A_r \approx 1.56$ mag for Galactic extinction.

In addition to the localization and candidate galaxies, one must also adopt a set of priors to perform the PATH analysis. We follow the preferred assumptions of Aggarwal et al. (2021), i.e. their inverse prior and exponential offset function with $\theta_{\max} = 6\phi$. For the unseen prior $P(U)$, we assume a value of 10 per cent based on the angular sky coverage of the stars in the field. The last two columns of Table 3 list the prior probabilities $P(O)$ and posterior probabilities $P(O|x)$ for each of the galaxy candidates. The PATH results clearly favour J173438.35-504550.4 as the host of FRB 20201123A with a posterior probability $P(O|x) = 0.92$. We caution, however, that given the uniform localization of this FRB, this result is primarily driven by its bright flux and large angular size. Nevertheless, we proceed with relatively high confidence in this association (e.g. its posterior probability exceeds that of every other candidate by an order-of-magnitude).

5.3.2 Putative Host Analysis

Adopting J173438.35-504550.4 as the putative host galaxy for FRB 20201123A, we now proceed to measure its properties and compare these to other, secure FRB hosts (Heintz et al. 2020; Bhandari et al. 2022). Fig. 7 shows a spectrum of J173438.35-504550.4 obtained on UT 2021 March 24 with the Goodman spectrograph (Clemens, Crain & Anderson 2004) on the SOAR telescope as part of

Table 3. Sources within the localization region of FRB201123 and their properties. ϕ is the half-light radius as defined by PATH and the r -band magnitudes m_r are not corrected for Galactic extinction. $P(O)$ and $P(O|x)$ are the prior and posterior probabilities, respectively, for each galaxy candidate.

RA ($^{\circ}$)	Dec ($^{\circ}$)	ϕ ($''$)	m_r (mag)	object classifier	$P(O)$	$P(O x)$
263.66814	-50.76320	0.30	18.6	0.99	0.000	0.000
263.66655	-50.76323	0.18	20.9	0.98	0.000	0.000
263.65963	-50.76407	1.75	16.5	0.03	0.838	0.915
263.67147	-50.76451	0.24	20.1	0.98	0.000	0.000
263.65821	-50.76454	0.20	20.9	-	0.006	0.008
263.67429	-50.76465	0.22	20.3	0.98	0.000	0.000
263.66691	-50.76538	0.19	20.9	0.99	0.000	0.000
263.65972	-50.76561	0.15	21.7	-	0.003	0.004
263.67249	-50.76610	0.34	17.8	0.99	0.000	0.000
263.66119	-50.76641	0.21	20.6	-	0.008	0.011
263.65584	-50.76682	0.26	19.4	0.98	0.000	0.000
263.67210	-50.76691	0.23	20.1	0.98	0.000	0.000
263.67667	-50.76731	0.15	21.5	0.98	0.000	0.000
263.66322	-50.76732	0.63	22.2	-	0.002	0.002
263.66439	-50.76746	0.19	20.7	0.98	0.000	0.000
263.65874	-50.76765	0.29	18.9	0.99	0.000	0.000
263.66397	-50.76782	0.29	18.9	0.98	0.000	0.000
263.66740	-50.76814	0.52	15.6	0.96	0.000	0.000
263.66128	-50.76787	0.24	20.0	0.88	0.014	0.019
263.65673	-50.76838	0.35	17.7	0.98	0.000	0.000
263.67182	-50.76831	0.24	19.9	0.98	0.000	0.000
263.67399	-50.76835	0.24	19.9	0.98	0.000	0.000
263.66306	-50.76873	0.38	16.6	1.00	0.000	0.000
263.65996	-50.76859	0.31	18.6	0.98	0.000	0.000
263.67438	-50.76912	0.29	18.8	0.99	0.000	0.000
263.65887	-50.76920	0.30	18.7	0.98	0.000	0.000
263.67301	-50.76945	0.29	19.1	0.98	0.000	0.000
263.67363	-50.76963	0.16	21.2	0.98	0.000	0.000
263.66927	-50.76982	0.34	17.7	0.95	0.000	0.000
263.66560	-50.77039	0.28	19.3	0.84	0.030	0.041
263.66719	-50.77070	0.51	15.8	0.99	0.000	0.000
263.65809	-50.77129	0.28	19.2	0.98	0.000	0.000
263.66104	-50.77129	0.14	21.7	0.98	0.000	0.000
263.67622	-50.77218	0.18	20.8	0.98	0.000	0.000
263.67074	-50.77272	0.28	19.7	0.98	0.000	0.000
263.67280	-50.77278	0.23	20.0	0.98	0.000	0.000
263.65951	-50.76679	0.23	20.7	0.98	0.000	0.000
263.65988	-50.76690	0.20	20.9	0.98	0.000	0.000

program SOAR2021A-010. The instrument was configured with the 400_SZYZ grating, a 1.0 arcsec long slit, and 2×2 binning. These data were reduced with the PyeIt data reduction pipeline (Prochaska et al. 2020) and flux calibrated with a spectrophotometric standard requiring the r -band apparent magnitude to match that of the galaxy (to crudely correct for slit losses). For the figure and subsequent analysis, we have corrected the data for Galactic extinction, assuming a reddening $E(B - V) = 0.19$ mag and the Cardelli, Clayton & Mathis (1989) extinction law. The galaxy exhibits strong nebular emission lines at a common redshift $z = 0.0507$, including [OII], H β , [OIII], H α , and [NII].

We performed a stellar population fit to the data at wavelengths $\lambda_{\text{obs}} = 3700\text{--}7075\text{\AA}$ using the pPXF software package (Cappellari 2012). For the analysis, we followed the assumptions of previous works (e.g. Heintz et al. 2020). The results provide an estimate of the stellar mass ($M_* \approx 10^{11.2} M_{\odot}$) and the emission-line flux of H α ($f_{\text{H}\alpha} = 4.2 \times 10^{-15}$ ergs cm $^{-2}$ s $^{-1}$) with the latter yielding an inferred star formation rate of $\text{SFR} \approx 0.2 M_{\odot} \text{ yr}^{-1}$ after correcting

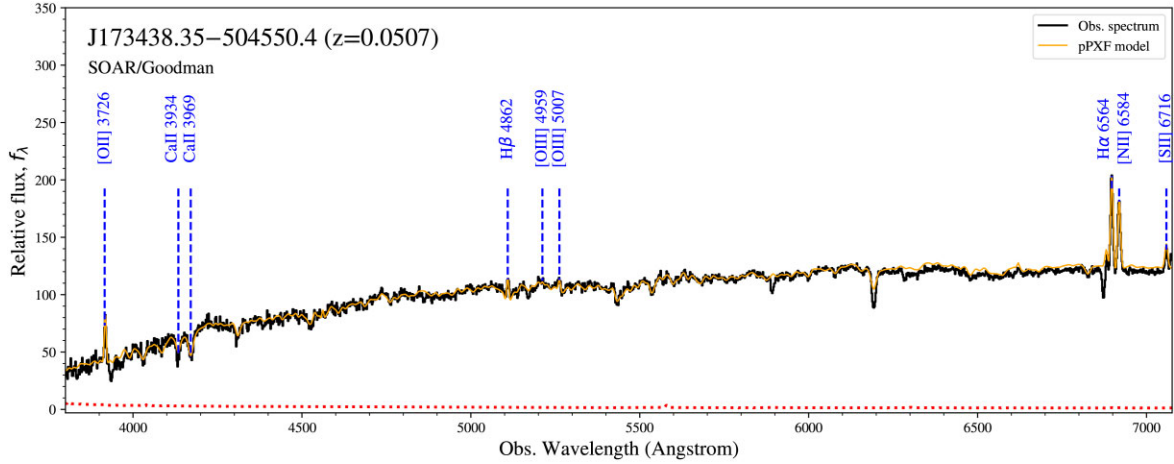


Figure 7. SOAR/Goodman optical spectrum of J173438.35-504550.4, the putative galaxy host of FRB 201123. The observed spectrum is shown by the black histogram and its uncertainty is shown by the red-dashed line. Some spectral features at a common redshift of $z = 0.0507$ have been highlighted in blue. Our adopted pPXF model is shown as a solid orange line. See Section 5.3.2 for further details.

for internal extinction with $A_V \approx 0.7$ mag based on the H_α/H_β ratio. Uncertainties in M_* and SFR are dominated by systematics, which include the assumed IMF, slit loss, and dust extinction (both galactic and internal). We estimate 0.3 dex errors for each quantity. The M_* and SFR values of J173438.35-504550.4 place it well within the locus of measured values of highly secure FRB host galaxies (Bhandari et al. 2022).

6 FLUENCE LIMITS

Apart from FRB 20201123A, we do not have accurate localization information on the newly discovered FRBs. This makes calculation of a fluence for the FRBs quite challenging. Hence, we estimate the lower limit on the fluences of the bursts if we assume that the FRB 20200413A and FRB 20200915A are close to the edge of the CB tiling pattern and FRB 20201123A is at the boresight of the CB in which it was discovered. Using the radiometer equation (Dewey et al. 1985), for an FRB with a signal-to-noise ratio S/N, the fluence,

$$\mathcal{F} = \frac{S/N T_{\text{sys}} \sqrt{W_{\text{meas}}}}{G \sqrt{n_p} \Delta\nu} \times 1000 \text{ Jy ms}, \quad (8)$$

where, T_{sys} is the system temperature, G is gain of the telescope in K Jy^{-1} , W_{meas} is the measured width of the FRB in seconds (after de-dispersion and after compensating for any other smearing effects), n_p is the number of polarizations summed and $\Delta\nu$ is the bandwidth of the receiver in Hz. Instrumental parameters for MeerKAT from Bailes et al. (2020) are $n_p = 2$, $\Delta\nu = 856$ MHz. We use a $G = 0.175 \text{ K Jy}^{-1}$ for FRB 20200413A and 0.3 K Jy^{-1} for FRB 20200915A after taking into account the reduction in the gain of the IB telescope due to the offset from the boresight. This is because the power level at which the CB tiling ends is different for the two FRBs. We assume a gain of 1.75 K Jy^{-1} for the CB of FRB 20201123A (modified from 2.8 K Jy^{-1} since only 40 out of 64 MeerKAT dishes were used for the observations). The telescope's system temperature T_{sys} is given by $T_{\text{sys}} = T_{\text{rec}} + T_{\text{sky}}$, with $T_{\text{sys}} = 18 \text{ K}$, the receiver temperature for the 1.4 GHz observations (Ridolfi et al. 2021). We assume the total sky temperature to be 23 K for all FRBs, assuming a mean of 5 K contribution due to the sky. Using these values, we obtain a lower limit on the fluence, $\mathcal{F} \gtrsim 3.1$ and 3 Jy ms for FRB 20200413A and FRB 20200915A, respectively. For FRB 20201123A, we also correct the S/N to account for the reduction in the gain of the CB due to its

offset from the boresight of the primary beam (18.072 arcmin). If we assume that FRB 20201123A originates from the host galaxy J173438.35-504550.4, we can compute the true fluence of the burst. In order to do that, we obtain the true gain of the CB at the optical centre of J173438.35-504550.4 by simulating the point spread function of the CB using MOSAIC (Chen et al. 2021).¹² We estimate G of 1.4 K Jy^{-1} and using this new value, we obtain $\mathcal{F} \gtrsim 1.4 \text{ Jy ms}$. The final limits are presented in Table 2. Given the redshift of J173438.35-504550.4, we estimate the lower limit on the energy of the burst in the MeerKAT band of $8.4 \times 10^{34} \text{ J}$. This luminosity is consistent with the general population of FRBs (Luo et al. 2018).

7 DISCUSSION

7.1 Limits on repeating bursts

Since MeerTRAP is a commensal survey instrument, there are always opportunities to follow-up newly discovered FRBs as the field is usually observed multiple times by the LSPs. This means that we were able to obtain follow-up of the fields to look for repeat bursts for the three FRBs reported in this paper. FRB 20201123A shows a post-cursor of about 200 ms after the initial bright burst, suggesting that it may be a repeater. Such post-cursor bursts have been observed in other repeating FRBs like FRB 20121102A (Zhang et al. 2018; Cruces et al. 2021) and could be a vital diagnostic to identify the nature of FRB 20201123A. So far, MeerTRAP has observed the same field for a total of 25.4 h. No other burst was detected at the same DM at the S/N threshold of 8.0. If we assume that FRB 20201123A is a repeating source and the burst arrival times are Poisson distributed (Cruces et al. 2021), one can obtain a 95 per cent confidence limit on the repeat rate for the effective sensitivity of the survey in that direction (assuming that it remains unchanged in that direction for successive observations). From Gehrels (1986), the 95 per cent confidence level upper limit on the repeat rate is given by

$$\mathcal{R}_{\text{ul}} = \frac{4.744}{t_{\text{obs}}}, \quad (9)$$

¹²<https://github.com/wchenastro/Mosaic>

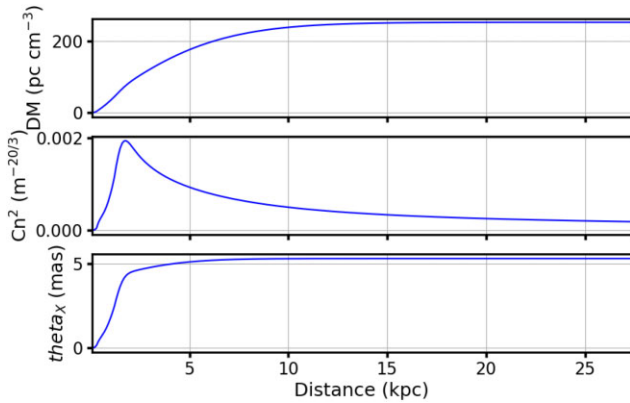


Figure 8. The expected galactic DM contribution (top panel), strength of scattering (middle panel), and angular broadening of extragalactic sources (bottom panel) as a function of distance from the Earth towards FRB 20201123A. The simulations were performed using NE2001 model (see text for more details).

where t_{obs} is the total observation time. This gives a limit on \mathcal{R}_{ul} of 0.18 bursts per hour. For the other two FRBs, the total time on sky is too low (< 2 h) to put any tight constraint on the repeat rate. We note that the gap between detection of the first event and the start of the follow-up observation is important to find repeat bursts (see Caleb et al. 2019, for more details) but since MeerTRAP does not have control over when the same field is observed, we can only provide rough limits on the repeat rate of these FRBs.

7.2 Scattering in FRB 20201123A

The spectral index of the scattering in FRB 20201123A (α) (the left-hand panel of Fig. 3) is -4.2 , which is consistent within $1\text{--}\sigma$ errorbars to the $\nu^{-4.4}$ relationship that is expected for a turbulent medium that follows a Kolmogorov spectrum (e.g. Lorimer & Kramer 2004). In order to determine the predicted scattering contribution from the Milky Way, we looked at the expected values from the electron density models of our Galaxy along this line of sight (Cordes & Lazio 2002; Yao, Manchester & Wang 2017). For an FRB at a distance D and a scattering screen distance, d_{screen} , $\tau \simeq \frac{\theta^2 d_{\text{screen}}^2}{8ln(2)c}$ where θ is the extragalactic angular broadening and c is the speed of light (see Main et al. 2021, and the references therein). We took 100 randomly sampled RA and Dec within a 30×30 arcsec circle around the centre of the CB in which FRB 20201123A was detected and computed the total scattering measure and the DM contribution of our Galaxy as a function of distance using the electron density models. Fig. 8 shows the values of C_n^2 (the measure of scattering strength) and the DM contribution, and one can clearly see that the maximum contribution to scattering comes from a putative screen at a distance of 1.8 kpc. Using $\theta \sim 5.314$ mas gives $\tau \sim 22 \mu\text{s}$ at 1 GHz. The YMW16 model (Yao et al. 2017) reports an expected scattering time-scale of $150 \mu\text{s}$ which is still two orders of magnitude lower than the measured $\tau \sim 10$ ms at 1 GHz, suggesting that the scattering cannot originate from our Galaxy. This means that the scattering in this FRB might originate from an extremely turbulent medium close to the FRB itself, as is inferred from the current FRB population (see Chawla et al. 2021).

Another possibility that we considered was that the majority of the scattering originates from an intersecting halo of a foreground galaxy (see Prochaska et al. 2019, for more details). While it is expected that the gas in the haloes of galaxies is not dense, the

geometric boost under the thin screen-scattering model may render an intervening halo to dominate the scattering comparable to turbulent environments in the host or our Galaxy if it is between the host galaxy and us. In order to quantify how likely it is that the sightline is intersected by foreground haloes, we follow the same technique as presented in Prochaska et al. (2019). We use the Aemulus Halo Mass function (McClintock et al. 2019) to generate haloes of masses between $2 \times 10^{10} M_{\odot}$ and $10^{16} M_{\odot}$. Then, we compute the average number of haloes in the co-moving volume enclosed at the redshift of the host galaxy of FRB 20201123A ($z = 0.0507$), $N(z) = 0.227$. Then, assuming the impact parameter of the FRB line of sight to be comparable to the virial radius of the intervening galaxy and assuming that the haloes are Poisson distributed in the given co-moving volume, the probability that the sightline is intersected by k haloes,

$$P(k|N(z)) = \frac{N^k e^{-N}}{k!}. \quad (10)$$

Hence, the probability of intersecting at least one halo, $P(k \geq 1|N(z))$ is $1 - e^{-N}$, which is ~ 21 per cent. The value of $P(k \geq 1|N(z))$ is sensitive to the value of $N(z)$, which in turn depends on the lowest halo mass assumed in the Halo Mass function. If we assume that the lower limit on the halo mass comes from the halo of a Milky Way like galaxy ($10^{12} M_{\odot}$), we get $N(z)$ of 0.099, which reduces $P(k \geq 1|N(z))$ by a factor of 2. Regardless, this is a non-negligible probability and allows that the scattering could originate from multiple intersecting haloes of foreground galaxies.

In order to distinguish between the two possibilities, we predict the scattering that would be induced if it was originating in the host or in an intervening galaxy. Based on previous work by Ocker, Cordes & Chatterjee (2021), the expected scattering time,

$$\tau(\nu, \text{DM}, z) \simeq 48.03 \frac{A_{\tau} \tilde{F} G \text{DM}_1^2}{(1+z_l)^3 \nu^4} \mu\text{s}, \quad (11)$$

where A_{τ} is a factor close to unity, \tilde{F} is the factor that characterizes the turbulence in the scattering medium, G is the geometric boosting to scattering due to the distance between the scattering screen, the source and the observer ($G \sim d_{l0} d_{s1} / L d_{so}$) where d_{s1} , d_{so} , and d_{l0} are the angular diameter distances of source to lens, source to observer, and lens to observer, respectively. DM_1 is the DM contribution from the scattering medium, z_l is the redshift of the scattering medium, and ν is the observing frequency. If the scattering originates in the host galaxy, we expect \tilde{F} to dominate the total scattering time while $G \sim 1$. On the other hand, if the scattering is dominated by the intervening galaxy halo, we expect G to be large ($G \simeq 2\delta d/L$) for $\delta d \gg L$, where δd is the distance from the lens to the source or the observer. In this case, we expect little to no turbulence from the diffuse gas as shown from previous studies (see Prochaska et al. 2019, for more details). Here, we compute the scattering for a foreground galaxy that lies at a distance ranging from 25 per cent to 75 per cent of the redshift of the host. For the host galaxy scattering, we assume $G \sim 1$ and compute scattering for various values of \tilde{F} . For scattering from an intervening halo, we used the smallest value of $\tilde{F} \sim 0.0001$ measured for pulsars in our Galaxy (Ocker et al. 2021) and computed scattering for various values of G derived from the range of distances of the intervening halo. We also evolve \tilde{F} with the star-formation rate using equation 21 in Ocker et al. (2022). We note that the value of \tilde{F} used is very conservative as \tilde{F} is expected to be even smaller but pulsars are unable to probe this diffuse gas. Fig. 9 shows the expected scattering for both scenarios. It is clear that the foreground galaxies cannot account for the scattering seen in FRB 20201123A (7.5 ms at 1 GHz) even for all possible values of G within the co-moving volume enclosed by the host galaxy of FRB 20201123A, while one

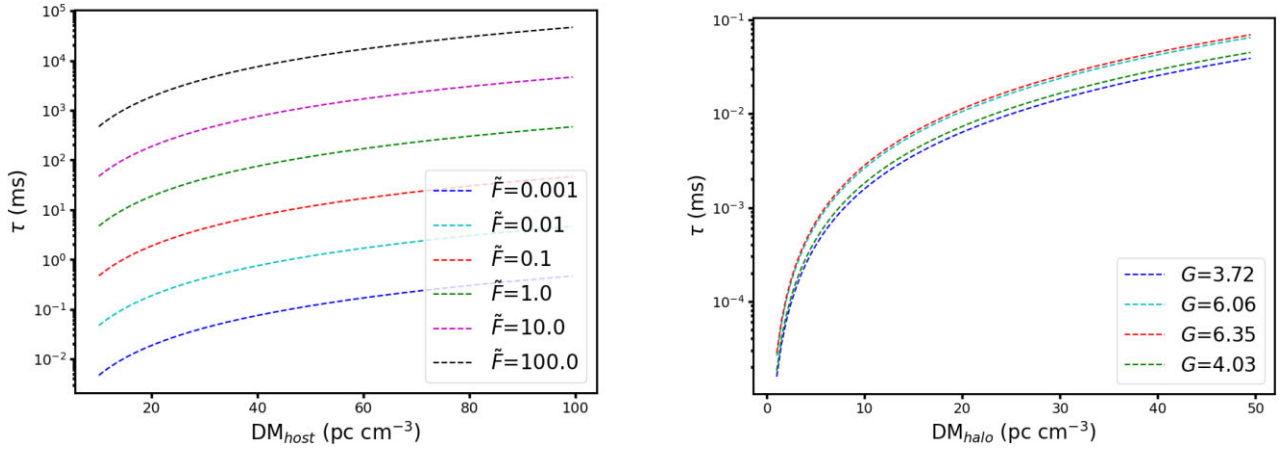


Figure 9. **Left-hand panel:** Scattering time (τ) at 1 GHz as a function of host DM contribution for various values of \tilde{F} that signifies turbulence for FRB 20201123A. **Right-hand panel:** τ at 1 GHz as a function of DM from the halo of an intervening galaxy for values of G (computed from a range of redshifts between 0 and 0.0507) that signifies the geometric boosting to scattering. The analysis is done for a lens with a size of 0.03 Mpc.

can obtain the expected τ at 1 GHz from the host galaxy itself fairly easily. Hence, we conclude that the scattering in this FRB originates from the host galaxy.

7.3 Host galaxy of FRB 20201123A

Along with the time-domain detections, we identified J173438.35-504550.4 as a potential host galaxy for FRB 20201123A using robust statistical treatment given the relatively small localization error region. At face value, the low redshift of J173438.35-504550.4 appears at odds with the large dispersion measure for FRB 20201123A ($DM_{\text{FRB}} \approx 434 \text{ pc cm}^{-3}$). Our Galaxy, however, contributes $DM_{\text{ISM}} \approx 200 \text{ pc cm}^{-3}$ (NE2001 gives 229 pc cm^{-3} and YMW16 gives 162 pc cm^{-3}) from its interstellar medium and a presumed $DM_{\text{Halo}} \sim 50 \text{ pc cm}^{-3}$ from its halo (Prochaska & Zheng 2019). This leaves $\approx 180 \text{ pc cm}^{-3}$ for the cosmos (DM_{cosmic}) and the host (DM_{host}). At $z = 0.05$, the average cosmic contribution is $\langle DM_{\text{cosmic}} \rangle \sim 42 \text{ pc cm}^{-3}$ (Macquart et al. 2020) but the intrinsic scatter in this quantity is predicted to be large. Adopting the best-fitting model to the Macquart relation by Macquart et al. (2020), the 95 per cent confidence interval is $DM_{\text{cosmic}} = [15, 125] \text{ pc cm}^{-3}$. Allowing for the maximum value of this interval (which would imply a significant foreground galaxy halo), we recover a minimum host contribution of $DM_{\text{host,min}} \approx 60 \text{ pc cm}^{-3}$. This is consistent with estimates for host galaxy contributions from theoretical and empirical treatments (Prochaska & Zheng 2019; James et al. 2022). For a true DM_{cosmic} value of this sightline closer to (or below) the mean, the host contribution would exceed 100 pc cm^{-3} . Such values are inferred for other FRB hosts (e.g. FRB 20121102A; Tendulkar et al. 2017). In conclusion, we find no strong evidence to rule out the association with J173438.35-504550.4 based on its redshift and DM_{FRB} . The significant host contribution to the DM, combined with the scattering in FRB 20201123A possibly originating in the host, shows that it shares similarities with other highly active, repeating FRBs like FRB 20121102A and FRB 20190520A and potentially resides in a turbulent and dense environment within the host.

7.4 Speckled emission of FRB 20200915A

As mentioned previously, we see speckled emission in the dynamic spectrum of FRB 20200915A, whose frequency evolution may not

vary with interstellar scintillation from our Galaxy. A more robust method of confirming this conjecture would be to fit the scintles analytically to show how the width varies with frequency. In the case of FRB 20200915A, the scintles are not bright enough or do not conform to a specific shape such that they could be fit by an analytical model. Hence, the disagreement with Galactic scintillation can only be marginally validated visually in this case. Another possibility is that the speckled behaviour may arise from plasma lensing of FRB emission in the vicinity of the progenitor giving rise to caustics that are observed in the dynamic spectrum. The caustics are chromatic in nature and can manifest themselves as magnified islands of emission in time and observed frequency space (see Cordes et al. 2017; Main et al. 2018, for more details). Within a perfect-lens approximation, the frequency width of a caustic due to magnification from a 1D elliptical lens,

$$\frac{\Delta\nu}{\nu} \propto \frac{R_1^2}{\Delta x^2}, \quad (12)$$

where R_1 is the equivalent radius ($R_1 = R_{\text{fr}}/\sqrt{\pi}$ where R_{fr} is the Fresnel scale) of the lens in the circular approximation and Δx is the semi-major axis of the lens. One caveat here is that the relative velocity between the source and lens will cause the waves to interfere and produce complex patterns in the frequency space that can manifest itself as islands of emission drifting in time and frequency. Since we do not see any drift in time as seen for other repeating FRBs (Hessels et al. 2019), we can only put an upper limit on the velocity of the plasma lens in the x -direction with respect to the FRB. The relative velocity,

$$v \geq 0.5 \frac{R_1}{\Delta t} \left(\frac{\Delta\nu}{\nu} \right)^{0.5}, \quad (13)$$

where the delay in obtaining a new caustic due to the relative motion is,

$$\Delta t \geq 0.7 \frac{R_1^2}{v \Delta x}. \quad (14)$$

In our case, Δt is constrained by the maximum dispersion smearing in our band which corresponds to 3.4 ms for FRB 20200915A. Assuming the size of the filament close to the FRB of $\sim 1 \text{ AU}$, we get $R_1 \sim 100 \text{ km}$. Using these values in equation (13) gives a lower limit on v of $4.6 \times 10^2 \text{ km s}^{-1}$. Regardless of which model we consider, they cannot explain the decrease in the spectral extent of

the emission with increasing frequency. Thus, we conclude that the speckled emission seen in FRB 20200915A might be intrinsic to the FRB. Such speckled emission has also been observed in a number of FRBs discovered by ASKAP (Shannon et al. 2018) and could point to a common emission characteristic within the population. However, as mentioned previously, we cannot rule out weak scintillation arising from the halo of an intervening galaxy as confirming the same would require data at much higher time resolution.

8 SUMMARY

In summary, we present the first three discoveries of FRBs from the MeerTRAP project. FRB 20200915A shows speckled emission structure in the dynamic spectrum that is reminiscent of a few FRBs discovered by ASKAP. We show that the decorrelation bandwidth of the scintles of FRB 20200915A does not seem to follow the typical ν^4 frequency relation and also cannot be explained by plasma lensing in the host galaxy, suggesting that the speckled nature of the burst might be intrinsic in nature. FRB 20201123A shows clear evidence for scattering. We investigated the origin of scattering in FRB 20201123A and find that the scattering cannot originate from our Galaxy or the halo of an intervening galaxy and is most likely dominated by some turbulent material in close proximity to the source, as expected from recent simulations by Chawla et al. (2021). As FRB 20201123A was detected only in a single coherent beam, we were able to put tight constraints on its location. Using the non-detection in adjacent beams and a Bayesian framework called PATH, we were able to hone in on the most probable host galaxy for FRB 20201123A. Assuming J173438.35-504550.4 to be the host of FRB 20201123A, the DM contribution from the host is still consistent with what one would expect for the host galaxy contribution to the DM, which can exceed 100 pc cm^{-3} for the smallest contribution from the IGM based on the Macquart relation. This combined with the scattering suggests some similarities between the environment of FRB 20201123A and few of the prolific repeating FRBs. None of the bursts were seen to repeat although a faint post-cursor was seen 200 ms after the main burst of FRB 20201123A.

ACKNOWLEDGEMENTS

The authors would like to thank the anonymous referee whose comments significantly improved the manuscript. K.M.R., B.W.S., M.C., F.J., M.S., T.B., L.D., S.S., M.M., and V.M. thank the MeerKAT Large Survey Project teams for allowing MeerTRAP to observe commensally. K.M.R., B.W.S., M.C., F.J., M.S., T.B., L.D., S.S., M.M., and V.M. acknowledge funding from the European Research Council (ERC) under the European Union's Horizon 2020 - research and innovation framework programme (grant agreement No. 694745). The authors also acknowledge the usage of TRAPUM infrastructure funded and installed by the Max-Planck-Institut für Astronomie and the Max-Planck-Gesellschaft. The authors would like to thank Christopher Williams and Aris Karastergiou for invaluable help during the commissioning of the MeerTRAP system. K.M.R. acknowledges support from the Vici research program 'ARGO' with project number 639.043.815, financed by the Dutch Research Council (NWO). M.C. acknowledges support of an Australian Research Council Discovery Early Career Research Award (project number DE220100819) funded by the Australian Government and the ARC Centre of Excellence for All Sky Astrophysics in 3 Dimensions (ASTRO 3D), through project number CE170100013. J.K.K. acknowledges support from the Swiss National Science Foundation under grant 185692. Authors W.F., C.K., J.X.P., and N.T. as members

of the Fast and Fortunate for FRB Follow-up team, acknowledge support from NSF grants AST-1911140 and AST-1910471. N.T. and C.N. acknowledge support by FONDECYT grant 11191217. The authors would like to thank Rene Breton for invaluable discussions regarding the localization of FRB 20201123A using the Bayesian Framework. The MeerKAT telescope is operated by the South African Radio Astronomy Observatory (SARAO), which is a facility of the National Research Foundation, an agency of the Department of Science and Innovation. The authors would also like to thank the South African Radio Astronomy Observatory staff for all the help during these observations. Based on observations obtained at the international Gemini Observatory, a program of NSF's NOIRLab, which is managed by the Association of Universities for Research in Astronomy (AURA) under a cooperative agreement with the National Science Foundation on behalf of the Gemini Observatory partnership: the National Science Foundation (United States), National Research Council (Canada), Agencia Nacional de Investigación y Desarrollo (Chile), Ministerio de Ciencia, Tecnología e Innovación (Argentina), Ministério da Ciência, Tecnologia, Inovações e Comunicações (Brazil), and Korea Astronomy and Space Science Institute (Republic of Korea). The Gemini data were obtained from program GS-2021A-Q-134, and were processed using the DRAGONS (Data Reduction for Astronomy from Gemini Observatory North and South) package. The MALS data were processed using the MALS computing facility at IUCAA (<https://mals.iucaa.in>).

DATA AVAILABILITY

The data will be made available upon reasonable request to the authors. The galaxy observations of J173438.35-504550.4 are available at <https://github.com/FRBs/FRB>.

REFERENCES

- Adámek K., Armour W., 2020, *ApJS*, 247, 56
 Aggarwal K., Budavári T., Deller A. T., Eftekhari T., James C. W., Prochaska J. X., Tendulkar S. P., 2021, *ApJ*, 911, 95
 Armour W. et al., 2011, in Ballester P., Egret D., Lorente N. P. F., eds, ASP Conf. Ser. Vol. 461, A GPU-based Survey for Millisecond Radio Transients Using ARTEMIS. Astron. Soc. Pac., San Francisco, p.33
 Asad K. M. B. et al., 2021, *MNRAS*, 502, 2970
 Bailes M. et al., 2020, *PASA*, 37, e028
 Barr E. D., 2018, in Weltevrede P., Perera B. B. P., Preston L. L., Sanidas S., eds, Proc. IAU Symp. 337, Pulsar Astrophysics the Next Fifty Years. Kluwer, Dordrecht, p. 175
 Bertin E., Arnouts S., 1996, *A&AS*, 117, 393
 Bezuidenhout M. C. et al., 2022, *MNRAS*, 512, 1483
 Bhandari S., et al., 2022, *ApJ*, 163, 20
 Bochenek C. D., Ravi V., Belov K. V., Hallinan G., Kocz J., Kulkarni S. R., McKenna D. L., 2020, *Nature*, 587, 59
 Bradley L. et al., 2021, *astropy/photutils*: 1.1.0
 Briggs D. S., 1995, American Astronomical Society Meeting Abstracts. p. 112.02
 CHIME/FRB Collaboration et al., 2020, *Nature*, 587, 54
 Caleb M., Stappers B. W., Rajwade K., Flynn C., 2019, *MNRAS*, 484, 5500
 Caleb M. et al., 2020, *MNRAS*, 496, 4565
 Cappellari M., 2012, pPXF: Penalized Pixel-Fitting stellar kinematics extraction, (ascl:1210.002)
 Cardelli J. A., Clayton G. C., Mathis J. S., 1989, *ApJ*, 345, 245
 Chawla P., et al., 2021, *ApJ*, 927, 19
 Chen W., Barr E., Karuppusamy R., Kramer M., Stappers B., 2021, Journal of Astronomical Instrumentation, 10, 3
 Chime/Frb Collaboration et al., 2020, *Nature*, 582, 351

- Clemens J. C., Crain J. A., Anderson R., 2004, in Moorwood A. F. M., Iye M., eds, *Society of Photo-Optical Instrumentation Engineers (SPIE) Conference Series Vol. 5492, Ground-based Instrumentation for Astronomy*. p. 331
- Cordes J. M., Lazio T. J. W., 2002, preprint(astro-ph/0207156)
- Cordes J. M., Rickett B. J., 1998, *ApJ*, 507, 846
- Cordes J. M., Wasserman I., Hessels J. W. T., Lazio T. J. W., Chatterjee S., Wharton R. S., 2017, *ApJ*, 842, 35
- Cruces M. et al., 2021, *MNRAS*, 500, 448
- Dewey R. J., Taylor J. H., Weisberg J. M., Stokes G. H., 1985, *ApJ*, 294, L25
- de Villiers M. S., Cotton W. D., 2022, *AJ*, 163, 135
- Eatough R. P., Keane E. F., Lyne A. G., 2009, *MNRAS*, 395, 410
- Gaia Collaboration et al., 2018, *A&A*, 616, A1
- Gehrels N., 1986, *ApJ*, 303, 336
- Gupta N. et al., 2016, *Proceedings of MeerKAT Science: On the Pathway to the SKA*. p. 14
- Gupta N. et al., 2021, *ApJ*, 907, 11
- Heintz K. E. et al., 2020, *ApJ*, 903, 152
- Hessels J. W. T. et al., 2019, *ApJ*, 876, L23
- Hook I. M., Jørgensen I., Allington-Smith J. R., Davies R. L., Metcalfe N., Murowinski R. G., Crampston D., 2004, *PASP*, 116, 425
- Huchra J. P., Geller M. J., 1982, *ApJ*, 257, 423
- James C. W., Prochaska J. X., Macquart J. P., North-Hickey F., Bannister K. W., Dunning A., 2022, *MNRAS letters*, 510, L18
- Jankowski F. et al., 2020, preprint (arXiv:2012.05173)
- Jonas J., MeerKAT Team, 2016, *Proceedings of MeerKAT Science: On the Pathway to the SKA*. p. 1
- Lindgren L. et al., 2018, *A&A*, 616, A2
- Lorimer D. R., Kramer M., 2004, *Handbook of Pulsar Astronomy*. Cambridge observing handbooks for research astronomers Vol. 4
- Lorimer D. R., Bailes M., McLaughlin M. A., Narkevic D. J., Crawford F., 2007, *Science*, 318, 777
- Luo R., Lee K., Lorimer D. R., Zhang B., 2018, *MNRAS*, 481, 2320
- Macquart J.-P., Koay J. Y., 2013, *ApJ*, 776, 125
- Macquart J. P. et al., 2020, *Nature*, 581, 391
- Main R. et al., 2018, *Nature*, 557, 522
- Main R. A., Hilmarsson G. H., Marthi V. R., Spitler L. G., Wharton R. S., Bethapudi S., Li D. Z., Lin H. H., 2021, *MNRAS*, 509, 3172
- Majid W. A. et al., 2021, *ApJ*, 919, L6
- Malenta M. et al., 2020, in Pizzo R., Deul E. R., Mol J. D., de Plaa J., Verkouter H., eds, *ASP Conf. Ser. Vol. 527. Accelerating Radio Astronomy With High Performance Computing*. p. 457
- McClintock T. et al., 2019, *ApJ*, 872, 53
- Ocker S. K., Cordes J. M., Chatterjee S., 2021, *ApJ*, 911, 102
- Ocker S. K. et al., 2022, *ApJ*, 931, 11
- Onken C. A. et al., 2019, *PASA*, 36, e033
- Oswald L. S. et al., 2021, *MNRAS*, 504, 1115
- Platts E., Weltman A., Walters A., Tendulkar S. P., Gordin J. E. B., Kandhai S., 2019, *Phys. Rep.*, 821, 1
- Pleunis Z. et al., 2021, *ApJ*, 923, 1
- Prochaska J. X., Zheng Y., 2019, *MNRAS*, 485, 648
- Prochaska J. X. et al., 2019, *Science*, 366, 231
- Prochaska J. et al., 2020, *The Journal of Open Source Software*, 5, 2308
- Qiu H. et al., 2020, *MNRAS*, 497, 1382
- Rajwade K. M. et al., 2020, *MNRAS*, 495, 3551
- Ravi V. et al., 2016, *Science*, 354, 1249
- Rickett B. J., 1970, *MNRAS*, 150, 67
- Ridolfi A. et al., 2021, *MNRAS*, 504, 1407
- Sanidas S., Caleb M., Driessen L., Morello V., Rajwade K., Stappers B. W., 2018, in Weltevrede P., Perera B. B. P., Preston L. L., Sanidas S., eds, *Pulsar Astrophysics the Next Fifty Years*. Vol. 337, Cambridge University Press, Cambridge, UK, 406
- Shannon R. M. et al., 2018, *Nature*, 562, 386
- Spitler L. G. et al., 2016, *Nature*, 531, 202
- Tendulkar S. P. et al., 2017, *ApJ*, 834, L7
- The CHIME/FRB Collaboration et al., 2021, *ApJS*, 257, 41
- Thornton D. et al., 2013, *Science*, 341, 53
- Yao J. M., Manchester R. N., Wang N., 2017, *ApJ*, 835, 29
- Zhang Y. G., Gajjar V., Foster G., Siemion A., Cordes J., Law C., Wang Y., 2018, *ApJ*, 866, 149
- ¹Jodrell Bank Centre for Astrophysics, University of Manchester, Oxford Road, Manchester M13 9PL, UK
- ²ASTRON, the Netherlands Institute for Radio Astronomy, Oude Hoogeveensedijk 4, NL-7991 PD Dwingeloo, the Netherlands
- ³Sydney Institute for Astronomy, School of Physics, The University of Sydney, NSW 2006, Australia
- ⁴ASTRO3D: ARC Centre of Excellence for All-sky Astrophysics in 3D, Canberra 2601, ACT, Australia
- ⁵CSIRO, Space and Astronomy, PO Box 1130, Bentley, WA 6102, Australia
- ⁶Max-Planck-Institut für Radioastronomie, Auf dem Hügel 69, D-53121 Bonn, Germany
- ⁷South African Radio Astronomy Observatory, Black River Park, 2 Fir Street, Observatory, Cape Town, 7925, South Africa
- ⁸SKA Observatory, Jodrell Bank, Lower Withington, Macclesfield, SK11 9FT, United Kingdom
- ⁹Department of Physics and Astronomy, University of the Western Cape, Bellville, Cape Town, 7535, South Africa
- ¹⁰Observatoire de Paris, LERMA, Collège de France, CNRS, PSL Univ., Sorbonne Univ., F-75014 Paris, France
- ¹¹Center for Interdisciplinary Exploration and Research in Astrophysics (CIERA) and Department of Physics and Astronomy, Northwestern University, Evanston, IL 60208, USA
- ¹²Inter-University Centre for Astronomy and Astrophysics, Post Bag 4, Ganeshkhind, Pune 411 007, India
- ¹³National Radio Astronomy Observatory, 1003 Lopezville Road, Socorro, NM 87801, USA
- ¹⁴Department of Astronomy, University of Geneva, Chemin Pegasi 51, CH-1290 Versoix, Switzerland
- ¹⁵Institut d'Astrophysique de Paris, 98 bis boulevard, Arago, F-75014, Paris, France
- ¹⁶Franco-Chilean Laboratory for Astronomy, IRL 3386, CNRS and Departamento de Astronomía, Universidad de Chile, Casilla 36-D, Santiago, Chile
- ¹⁷Instituto de Física, Pontificia Universidad Católica de Valparaíso, Casilla 4059, Valparaíso, Chile
- ¹⁸University of California, Santa Cruz, 1156 High St, Santa Cruz, CA 95064, USA
- ¹⁹Kavli Institute for the Physics and Mathematics of the Universe, 5-1-5 Kashiwanoha, Kashiwa, 277-8583, Japan

This paper has been typeset from a $\text{\TeX}/\text{\LaTeX}$ file prepared by the author.